A general approach to the reconstruction of x-ray helical computed tomography

Jiang Hsieh

Citation: Medical Physics **23**, 221 (1996); doi: 10.1118/1.597706
View online: http://dx.doi.org/10.1118/1.597706
View Table of Contents: http://scitation.aip.org/content/aapm/journal/medphys/23/2?ver=pdfcov
Published by the American Association of Physicists in Medicine

A general approach to the reconstruction of x-ray helical computed tomography

Jiang Hsieh
Applied Science Laboratory, G.E. Medical Systems, Milwaukee, Wisconsin 53201

(Received 30 May 1995; accepted for publication 6 November 1995)

Helical Computed Tomography (HCT) has become the method of choice for many routine clinical studies. The advantages of HCT include the capability of scanning a complete anatomical volume in a single breath hold, the capability of generating images at any desired location, and the improved patient throughput. However, these advantages come at the expense of some image quality compromises. This is mainly caused by the fact that the projection set is inherently incomplete and inconsistent, due to the constant patient translation during the data acquisition process. In this paper, we will briefly review the research work performed in this area and present a more general approach to the problem. We give two specific examples of the general approach and compare the performance of one of the examples with one of the best methods available today. © *1996 American Association of Physicists in Medicine.*

I. INTRODUCTION

For years, x-ray computed tomography (CT) scans have been acquired with a step-and-shoot mode. The scanning process contains data acquisition (DA) and non-data acquisition (NDA) periods. During the DA period, the patient remains stationary while the x-ray tube (and the detector for the third generation systems) rotates about the patient to acquire a complete set of the projections. In the NDA period, the patient is indexed to the next scanning location. The NDA is typically on the order of seconds to minimize patient motion induced by the force of acceleration.[1,2] Compared to the DA period of one second, the duty cycle (or the scanning time efficiency) of the CT scanner is only 50% at best. In addition to a reduced patient throughput, this approach often results in a lack of complete anatomical organ coverage in a single breath hold.

With the recent advancement in CT scanners, a continuous data acquisition mode has been developed.[3,4] In this mode, the data is continuously acquired while the patient is translated at a constant speed. It is called helical or spiral scan (HCT), referring to the path of a point on the gantry with respect to a fixed reference point. The speed of the table increment is often described in terms of a helical pitch, instead of an absolute velocity.[9] A helical pitch is defined as the ratio of the distance that the table moves during 360° of gantry rotation to the slice thickness prescribed by the collimator. Therefore, a 1:1 helical pitch indicates that the distance between the first and the last views in any 360° gantry rotation is the same as the nominal slice thickness. This definition is convenient, not only for estimating the coverage of the patient, but also in defining the discrepancies in the projection dataset. Because the patient is indexed at a constant speed, there is no patient motion resulting from the force of acceleration or deceleration. HCT reduces the NDA to zero and a near 100% duty cycle is obtained.

There are several advantages associated with the HCT approach. First of all, it makes the complete volume coverage (e.g., a subvolume of a lung or the entire volume of a pancreas) in a single breath hold possible.[5–7] Clinically, this is very important in eliminating registration problems related to patient motion and reducing the contrast material uptake of the patient.[8] Another advantage of HCT is its ability to retrospectively select the plane of reconstruction at arbitrary locations, due to the volume scanning characteristics of the HCT, where each plane inside the scanning volume is equally sampled. (This is not the case, however, for the conventional CT, where the plane of reconstruction has to be identical to the plane of scanning.) This feature is particularly important when considering the case of isolating a small pathology. The ability to center the reconstructed slice at the object of interest will improve its contrast and visibility. Finally, HCT offers an improvement in patient throughput. The improvement is closely related to the helical pitch selection. In general, the higher the helical pitch, the faster that a volume can be covered and a CT study can be completed. Typically, a helical pitch of 1:1 is used for scanning bodies. A helical pitch as high as 2:1 is sometimes used when scanning time is critical.

Although HCT has many advantages, the quality of the image generated from the helical scan mode is, in general, inferior or at the best comparable to the images acquired with a step-and-shoot mode.[9] This is caused by the deviation from the basic tomographic reconstruction assumption that the projections should be collected from the same object. When the object is heterogeneous along the axis of translation, the attenuation distribution inside the scanning plane changes constantly. If proper correction is not rendered, undesirable image artifacts, such as shading or streaking, will result.

To overcome this difficulty, Mori suggested a scanning protocol of reduced helical pitch.[4] The projection data corresponding to consecutive 360° are averaged and weighted. The end result is equivalent to utilizing a larger slice thickness with a small helical pitch. Although this method is effective in reducing shading or streaking artifacts due to the data inconsistency, it is obtained at the expense of a reduced efficiency and volume coverage.

Nishimura and Miyazaki proposed a 4π interpolative al-

 0094-2405/96/23(2)/221/9/$6.00

gorithm to reduce the projection inconsistency error.[3] The method uses projections from two sets of 360° to estimate one set of projections at a constant location by linear interpolation. Although the method overcomes the shortcomings of reduced efficiency, as compared to the previously proposed scheme, it produces a significantly degraded slice profile.[9] Because the longitudinal resolution is an important issue in high resolution CT imaging, helical reconstruction algorithms that offer minimal slice broadening are desired.[10–13]

Crawford and King proposed a number of weighting schemes that reduce or eliminate errors caused by the constant table movement.[9] One type of weighting is derived so that a consistent half-scan is formed (the definition of a half-scan can be found in Ref. 14). In this method, moving data is acquired for view angles in the range $(0, 2\pi+4\gamma_m)$, where γ_m is the maximum detector angle. By linear interpolation of data on opposite sides of the slice plane, a set of stationary data in the range $(0,\pi+2\gamma_m)$ can be approximated. Since the method uses less than 4π data, the projections should contain less table and patient motion and the slice profile should be improved. However, the slice profile is still inferior to the ones that use only 2π projections.

Another weighting scheme makes use of the underscan and overscan algorithms that are currently employed in the step-and-shoot mode for patient motion reduction.[15,16] A key effect of table motion is a large discontinuity between data at angles 0 and 2π. This inconsistency can be minimized by underweighting the data near both ends of the scan. Since both algorithms use less than 4π views of data, they offer improved slice profiles.

One of the better weighting algorithms is the helical extrapolative (HE) algorithm.[17,9] The HE algorithm makes use of the fact that each projection set within 2π rotation can be divided into two sets of half-scans. By performing interpolation and extrapolation, a more consistent set of projections at a predefined slice plane can be obtained. Based on computer simulations and phantom studies, it was found that this method gives an overall best performance in terms of artifact reduction and slice profile.[9] Because of the nature of the fan beam geometry, the weighting function derived from the algorithm is discontinuous along a line in Radon space. To avoid any artifact caused by the discontinuity, a feathering algorithm is employed.

In this paper, we present a more general approach to the problem. Similar to the HE algorithm, projections of significantly less than 4π gantry rotation are employed in the reconstruction of an image. This will ensure the least degradation in slice profile. The major difference between our approach and the previously proposed schemes is the elimination of the plane of reconstruction constraint. As a result, the algorithm is interpolative and is therefore more stable than its extrapolative counterpart. Furthermore, the weighting function derived is continuous everywhere, and no feathering is required. Finally, the weights derived from this approach are exclusively in the range [0,1]. Therefore, a better noise property can be expected.

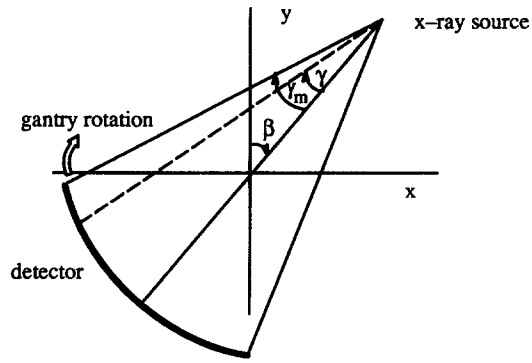

FIG. 1. Third generation scanner geometry.

II. THE GENERAL APPROACH

In this section, we will discuss a general approach to remove the artifacts that would be generated if a helical dataset were reconstructed without correction. For the purpose of illustration, we will give two specific examples and compare the performance of one of them against the HE algorithm. We hope that the example will demonstrate the advantages that the general approach offers as a result of the flexibility of the weight selection.

A. Scan geometry and data acquisition

For simplicity, we will limit our discussion to the third generation CT geometry.[18] The discussion can be easily extended to the fourth generation and the fan-parallel geometries.[19,20] Figure 1 shows the geometry of a third generation scanner. The source and the detector are stationary with respect to each other, while the entire apparatus rotates about the patient. Following existing convention, the scan plane is denoted $x-y$, and the direction normal to the scan plane is denoted by z. The view angle and detector angle are denoted by β and γ, respectively. For a conventional step-and-shoot mode, a projection ray can be uniquely defined by variables β and γ. In the case of a helical scan mode, however, the projection is also a function of the table location z. When the table is indexed at a constant speed, z is directly proportional to the view angle β and it is no longer an independent variable (note that since both β and z are linearly proportional to time t, there is a fixed linear relationship between β and z). Therefore, a projection can still be uniquely defined by $P(\beta,\gamma)$.

Although they differ tremendously in terms of theory and implementation, previously proposed weighting schemes have one important property in common: the plane of reconstruction (POR) is always placed halfway within the projection dataset and is always perpendicular to the axis of translation, as shown in Fig. 2. If we make the assumption that the error introduced in the projection measurement is proportional to the distance from POR, the selection of POR in the middle will minimize the overall inconsistency in the dataset. Note that the second constraint placed on POR is nothing but convention. It is inherited from the step-and-shoot scan

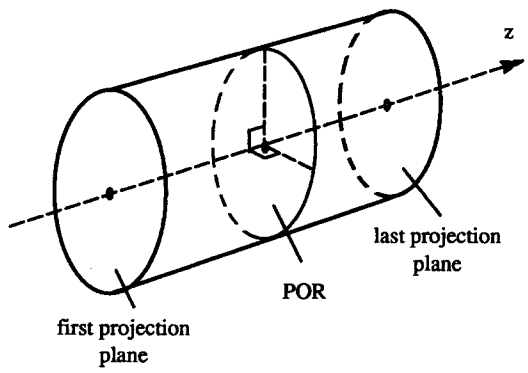

FIG. 2. Illustration of plane of reconstruction (POR).

mode, where POR is always perpendicular to the direction of patient translation (z axis). Furthermore, there is no logical reason to insist that POR has to be flat.

B. Review of the helical extrapolative (HE) algorithm

To fully understand the impact of the selection of POR on the weighting function, let us examine in detail the weights for the helical extrapolative (HE) algorithm.[9] The selection of the HE algorithm is based on the conclusion that it provides one of the best overall image quality (in terms of slice profile, artifact reduction, and noise performance) among different weighting schemes that were investigated. By examining it in detail, we could obtain some insight into the negative impact of the POR constraint on the property of the weighting function. Figure 3 shows a Radon space representation of projections with the horizontal axis representing the fan angle and the vertical axis representing the view angle. For the HE algorithm, POR is represented by line DC′. Note that the projections of 2π rotation contain two complete datasets (regions AEA′E′ and A′E′A″E″). The HE algorithm makes use of this data redundancy to minimize the impact of the starting and ending views by assigning less weights to these views. Since some of the redundant samples are located

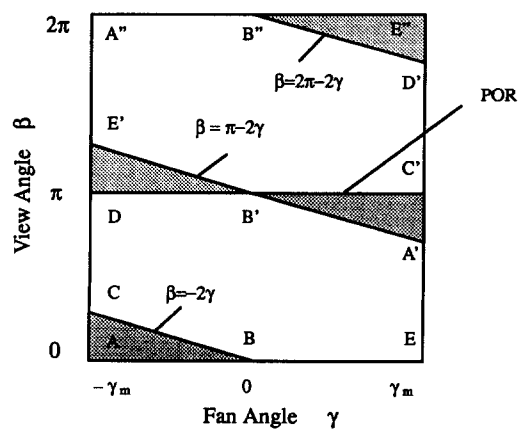

FIG. 3. Radon space for data acquired with the HE algorithm.

on the same side of POR (e.g., region ABC and A′B′C′), an extrapolative scheme has to be employed. The resulting weighting function is given by

$$w(\beta,\gamma)=\begin{cases}\dfrac{\beta+2\gamma}{\pi+2\gamma}, & 0\leq\beta\leq\pi-2\gamma,\\ \dfrac{2\pi-\beta-2\gamma}{\pi-2\gamma}, & \pi-2\gamma<\beta\leq 2\pi.\end{cases} \tag{1}$$

Note that the function $w(\beta,\gamma)$ is discontinuous in γ along the line $\beta=\pi-2\gamma$. This is mainly caused by the fact that POR is selected such that extrapolation has to be performed in regions A′B′C′ and DB′E′. In addition, because of the extrapolation, $w(\beta,\gamma)$ is less than zero in the two shaded triangles ABC and B″D′E″, and is larger than 1 in A′B′C′ and DB′E′. These weights will contribute to the increase in the noise, as compared to the weights that are in the range [0,1]. To eliminate the discontinuity, $w(\beta,\gamma)$ is feathered across the line $\beta=\pi-2\gamma$. The feathering of $w(\beta,\gamma)$ will destroy the property that the sum of the weights of the redundant sampling pair equal 1.

C. Region of reconstruction

Although the primary objective of the weighting scheme is to reduce the image artifact level caused by the projection data inconsistency, other factors that affect the overall image quality should also be considered. For example, it is well known that the noise characteristics changes with the selection of the weighting function.[21] Some of the weighting functions will generate patterned noise (photon statistics related) that have a distinct orientation, due to the variation of weights as function of β. The patterned noise often appears as a faint shower like pattern in a relatively uniform background (e.g., a liver). Although radiologists can "read through" it (since it does not mimic any pathology), the patterned noise is not a desirable feature. Another important parameter is the noise nonuniformity as a result of the weighting. Since most of the weights are detector channel dependent, the image noise contribution from the weights will, in general, be a function of γ (the 4π algorithm is one of the few exceptions[3]). In theory, we would like to preserve the noise level as uniform as possible across the entire field of view (FOV). Therefore, a weighting function that adds noise more uniformly would be preferred over the ones that significantly modulate the noise pattern. In addition, we would like to ensure the continuity of the weighting function in γ, since discontinuity could cause streaking artifacts in the image. Although it has been shown that feathering algorithm can be used to successfully bridge the discontinuity, it destroys the property that the weights of the complementary sampling pairs need sum up to unity. When we are restricted by the constraint that POR has to be perpendicular to the z axis and located halfway in the dataset, there is little flexibility in the selection of weights.

A more general approach to the problem is to define a "region of reconstruction" (ROR), as shown in Fig. 4. The ROR can be a warped plane or an irregularly shaped volume.

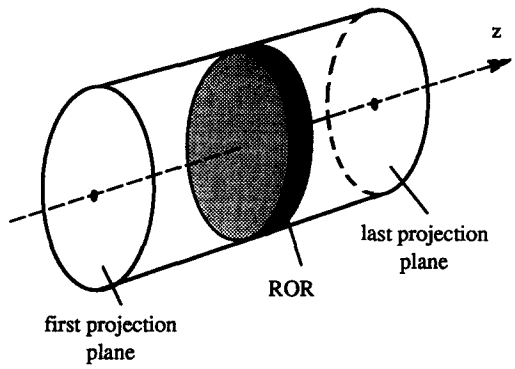

FIG. 4. Illustration of the region of reconstruction (ROR).

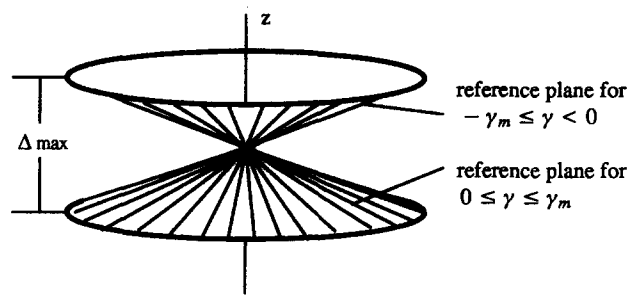

FIG. 6. An example of the ROR.

By eliminating the constraint that the projection estimation has to be performed with respect to a single flat plane perpendicular to the z axis, we gain the flexibility of being able to optimize the weighting function with respect to other image quality parameters. The optimization criteria can be based on noise uniformity, continuity, or smoothness of the weighting function, or other parameters that are deemed important to the image quality.

Let us now compare POR and ROR in Radon space. Assume the entire projection data is in the range $(0,2\theta)$. For the case of HE algorithm, $\theta=\pi$. For the case of a half-scan algorithm[9] $\theta=\pi+2\gamma_m$. Based on our previous discussion, the POR is a horizontal line located at $\beta=\theta$, as shown by the solid line in Fig. 5. The selection of ROR will extend the reference of interpolation in the β direction to cover an area indicated by the shaded region. This area could be a straight line at a angle, a curved line, or a region of nonzero width.

D. Two examples ROR

As the first example, let us select the ROR such that it overlaps with the line $\beta=\pi+\gamma_m-\gamma$ in the Radon space, as shown in Fig. 7. It can be shown that samples along this line form a set of parallel projections with a view angle $\pi+\gamma_m$.

In real space, ROR represents double cone shaped planes, as shown in Fig. 6. The interpolation for channels $0\leqslant\gamma\leqslant\gamma_m$ references the bottom portion of the double cone, and the channels $-\gamma_m\leqslant\gamma<0$ reference the top portion of the double cone. For the clarity of illustration, we have purposely magnified the extent of the double cone in the z direction. In reality, the maximum distance along z is very small. For example, for a 10 mm slice thickness and 1:1 pitch helical scan, Δ_{max} is only 1.25 mm. Intuitively, one would like to reduce Δ_{max} to its minimum to minimize the extent of the ROR in the z direction. Experiments have shown, however, that this is not of critical importance.

To derive a weighting function, let us examine the data sampling pattern in Radon space, as shown in Fig. 7. Let us denote by p_1 and p_2 a complementary sampling pair with z coordinates of z_1 and z_2. Further, let us denote the intersections of the ROR with two lines (parallel to z) passing through p_1 and p_2 by z_{r1} and z_{r2}. Following the operation of linear interpolation, the weighting factor, w_1, for point p_1 is given by

$$w_1=\frac{z_2-z_{r2}}{(z_2-z_{r2})+(z_{r1}-z_1)}. \tag{2}$$

Similarly, the weighting factor, w_2, for point p_2 is

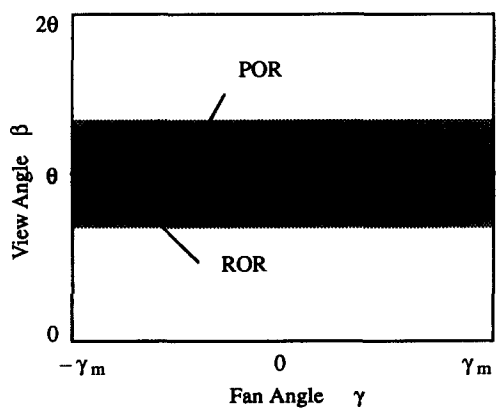

FIG. 5. Radon space representation of POR and ROR.

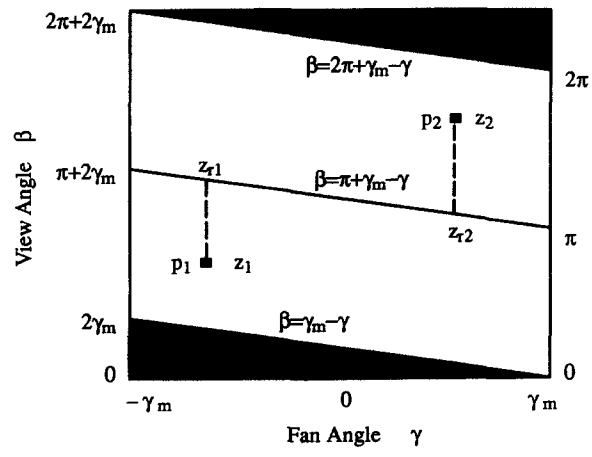

FIG. 7. Sampling pattern in Radon space for PI.

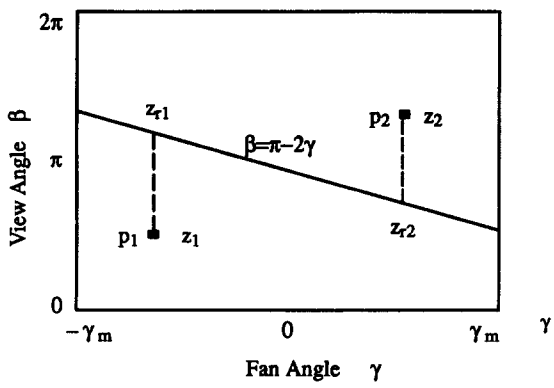

FIG. 8. Sampling pattern in Radon space for HI.

$$w_2=\frac{z_{r1}-z_1}{(z_2-z_{r2})+(z_{r1}-z_1)}. \tag{3}$$

Considering the fact that both the patient and the gantry move at constant speeds, the table position z is proportional to the projection angle β. We then have

$$w_1=\frac{\beta_2-\beta_{r2}}{\beta_2-\beta_1+\beta_{r1}-\beta_{r2}} \tag{4}$$

and

$$w_2=\frac{\beta_{r1}-\beta_1}{\beta_2-\beta_1+\beta_{r1}-\beta_{r2}}. \tag{5}$$

In order for the two sampling points to form a complementary sampling pair, the following relationship has to exist: $\beta_2=\beta_1+\pi+2\gamma_1$. Considering the fact that ROR is defined by $\beta=\pi+\gamma_m-\gamma$, we obtain

$$w(\beta,\gamma)=\begin{cases}\dfrac{\beta+\gamma-\gamma_m}{\pi}, & \gamma_m-\gamma\leq\beta\leq\pi+\gamma_m-\gamma,\\ \dfrac{2\pi+\gamma_m-\beta-\gamma}{\pi}, & \pi+\gamma_m-\gamma<\beta\leq 2\pi+\gamma_m-\gamma,\\ 0, \quad \text{otherwise.}\end{cases} \tag{6}$$

Note that $w(\beta,\gamma)$ reaches zero at both the beginning and ending views of the dataset ($\beta=\gamma_m-\gamma$ and $\beta=2\pi+\gamma_m-\gamma$ for the beginning and ending dataset, as shown in Fig. 7). In addition, the weighting function is continuous and equals to one along the line $\beta=\pi+\gamma_m-\gamma$. Therefore, $w(\beta,\gamma)$ is continuous everywhere. For the ease of future reference, we name this weighting function parallel interpolation (PI).

Now, let us consider a second example where ROR is selected, such that it overlaps with the line $\beta=\pi-2\gamma$, as shown in Fig. 8. The entire Radon space is nicely divided into two half-scan regions. In real space, the ROR is similar to that shown in Fig. 6. Following the same derivation, we obtain the following weighting function:

$$w(\beta,\gamma)=\begin{cases}\dfrac{\beta}{\pi-2\gamma}, & 0\leq\beta\leq\pi-2\gamma,\\ \dfrac{2\pi-\beta}{\pi+2\gamma}, & \pi-2\gamma<\beta\leq 2\pi.\end{cases} \tag{7}$$

Similarly, at the ROR ($\beta=\pi-2\gamma$), both equations equal 1. This indicates that the weighting function is continuous everywhere. It is also interesting to note that $w(\beta,\gamma)$ approaches zero when $\beta=0$ and $\beta=2\pi$. This is a desired property, since the inconsistency in the projections is expected to be the worst at both locations. In addition, the range of the equations is [0,1] in their respective domains. For the convenience of future reference, we name it the helical interpolative (HI) algorithm.

III. PERFORMANCE EVALUATION

To demonstrate the benefits of the added flexibility in selecting ROR, we performed detailed comparisons between the HI and the HE algorithms. Since both approaches used projection data in the same range $(0,2\pi)$, the comparison will be a direct measure of the performance of the weighting functions. We compare their performance in three major areas: noise performance, z-axis slice profile, and helical artifact suppression.

A. Noise performance

Since the projection will be multiplied by $w(\beta,\gamma)$ on a point by point basis, the noise power, $N(\gamma)$, of $w(\beta,\gamma)$ can be defined as the integration of the weighting function squared along β. (If a uniform phantom of cylindrical shape is scanned at the isocenter, the noise power will be a measure of noise increase for each channel due to the weighting process.) It can be easily shown that the noise power for the HI algorithm is

$$\begin{aligned}N_{\mathrm{HI}}(\gamma)&=\int_0^{2\pi}w^2(\beta,\gamma)d\beta\\&=\int_0^{\pi-2\gamma}\frac{\beta^2}{(\pi-2\gamma)^2}d\beta\\&\quad+\int_{\pi-2\gamma}^{2\pi}\frac{(2\pi-\beta)^2}{(\pi+2\gamma)^2}d\beta=\frac{2}{3}\pi.\end{aligned} \tag{8}$$

Note that the noise power is not a function of γ (the detector channel). In other words, the impact of multiplying the projection by $w(\beta,\gamma)$ is uniform across the entire detector. This property is desirable since the noise characteristics should be as homogeneous as possible. On the other hand, the noise power for the HE algorithm can be shown to be

$$N_{\mathrm{HE}}(\gamma)=\frac{\pi^3-8\gamma^3}{3(\pi+2\gamma)^2}+\frac{\pi^3+8\gamma^3}{3(\pi-2\gamma)^2}. \tag{9}$$

Obviously, the noise power is a function of γ (the detector channel). It is interesting to note that at the isochannel ($\gamma=0$), the noise powers for both algorithms are identical. As γ increases, N_{HE} is always higher than N_{HI}. This indicates that the HI algorithm will perform better in terms of noise sup-

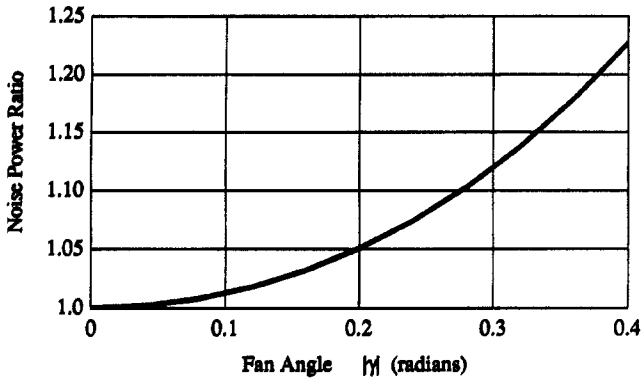

FIG. 9. Noise power ratio of HE over HI.

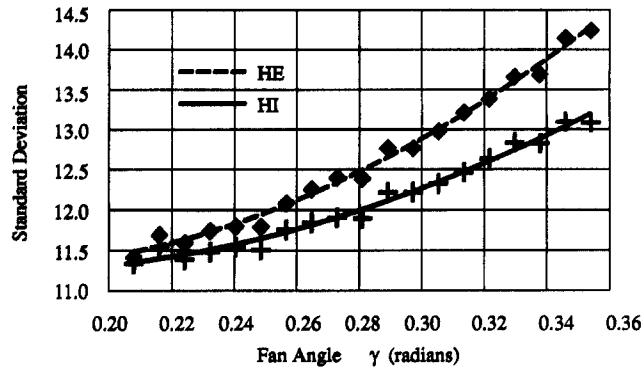

FIG. 10. Standard deviation measurement of a uniform phantom with HE and HI algorithms.

pression. Figure 9 depicts the ratio of N_{HE} over N_{HI} for the entire fan angle. At the edge of FOV, the HE algorithm is more than 20% higher in terms of noise measurement, as compared to the HI algorithm.

To confirm our analysis, we performed the following experiment. A uniform cylindrical phantom 48 in. in diameter was placed at the isocenter and scanned. The data was reconstructed with no weighting, HE weights, and HI weights. Since the phantom is uniform in z, no artifact associated with HCT should be observed. We want to perform the standard deviation measurement of the reconstructed images (in 40×40 pixel square regions) inside the phantom and map the measurements as function of γ (for the third generation CT scanner, there is an one to one relationship between the distance from the isocenter and the detector channel γ).

Note that any standard deviation measurement will include the estimation of photon related noise as well as any imperfection in the system. For example, small residual variations in the detector channel gains can produce rings in the reconstructed image. When the magnitudes of the rings are small, they can be masked by the photon noise and will not be observed visually. However, the rings will add errors to the standard deviation measurements. To overcome difficulties associated with the imperfect system calibration, we first subtracted the image generated with no weighting from the HE and HI images. We then performed standard deviation measurement on the difference images. Figure 10 shows the result of the experiment. The crosses and diamonds represent the actual measurements and the curves represent second-order polynomial fits to the measurement points. Note that the standard deviation associated with HE is consistently higher than that of HI, as predicated by the previous analysis. Figure 11 depicts the square of the ratio of the two fitted curves in Fig. 10. It is interesting to note that the variance ratio follows the noise power ratio quite nicely.

B. Slice profile

Because of the simultaneous translation motion of the patient, the slice profile of HCT is no longer determined solely by the x-ray focal spot size, collimation, and geometry. It also depends on the selection of the reconstruction algorithm. To compare the slice profiles of the HE and HI algorithms, we performed the following experiment. A 0.002 in. tungsten wire was placed at 45°, with respect to the z axis at three different locations: 0.5, 8.0, and 14.4 cm from the isocenter of the system. For each location, a HCT was performed with 5 mm collimation and 1:1 helical pitch. Both HE and HI weights were used during the reconstruction.

The wire was purposely placed at a steep angle with respect to the z axis for two reasons. First, a steeper angle will improve the accuracy of the slice profile measurement. Note that the calculation of the z-axis profile is based on the intersection of the wire with the slice. A shallower angle will reduce the slice profiles in the x-y plane. For the angle of 45°, the magnification factor is 1. The second consideration for the wire angle is the image artifact evaluation. In general, a wire placed at a steeper angle will produce worse artifacts than a wire at a shallow angle (when the wire is placed parallel to the z axis, no helical related artifact will be present).

To illustrate the appearance of the helical artifacts, we reconstructed images without any weighting, as shown in the left column of Fig. 12. Some shading artifacts can be clearly observed near the 6 and 12 o'clock positions. Not surpris-

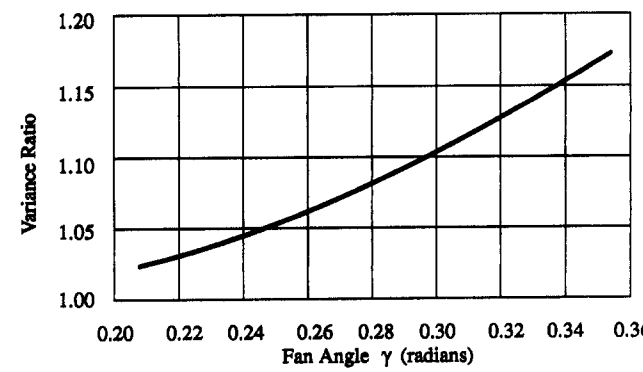

FIG. 11. Ratio of variance of HE over HI.

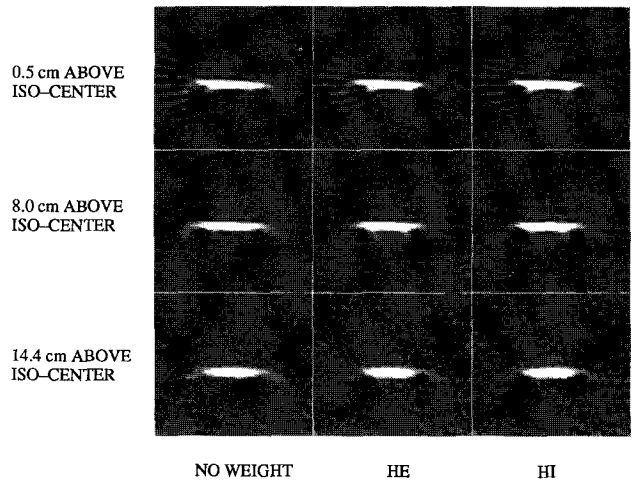

FIG. 12. Reconstructions of a tilted wire.

ingly, this is closely related to the starting scan position. We then performed HE and HI weighting to the same scan data and the reconstructed images are shown in the middle and the right columns of Fig. 12. Although some distortion can still be observed at the edge of the wire, they are less in intensity and more symmetrical. It is worth noting that the images produced by HE and HI algorithms are almost identical.

C. Artifact suppression

There are various helical related image artifacts. We have performed image artifact analysis on various phantoms and clinical studies. The results of the studies have been very consistent. Due to the limited scope of this paper, we will only present one example.

We selected a human skull phantom and scanned it near the base of the brain region. In this area, the anatomical structure changes quickly in the z direction to produce various helical related artifacts (shading and streaking). Therefore, it will be a good test of the algorithm's ability to suppress artifacts related to the projection inconsistencies as a result of the table movement. The phantom was first scanned in an axial scan mode (no table motion during scan) and then scanned in a helical mode with 1:1 pitch. In both cases, a 5 mm collimation was used. The image generated with the axial scan is used as the "gold standard" for artifact comparison, as shown in Fig. 13(a). For the ease of artifact identification, we reconstructed the helical scan without any correction, as shown in Fig. 13(b). Severe shading and streaking can be easily observed along the direction of the starting and ending view angles. This is not surprising, since the distance in z between these views is maximum and therefore produces the least consistency. Figures 13(c) and 13(d) depict images reconstructed with HE and HI algorithms. It is clear from the figure that most of the artifacts have been greatly reduced or eliminated. Visually, the two images are very similar in terms of their artifact reduction level. To quantitatively evaluate their artifact reduction capabilities, we performed region of interest (ROI) analysis for a number of locations. For each

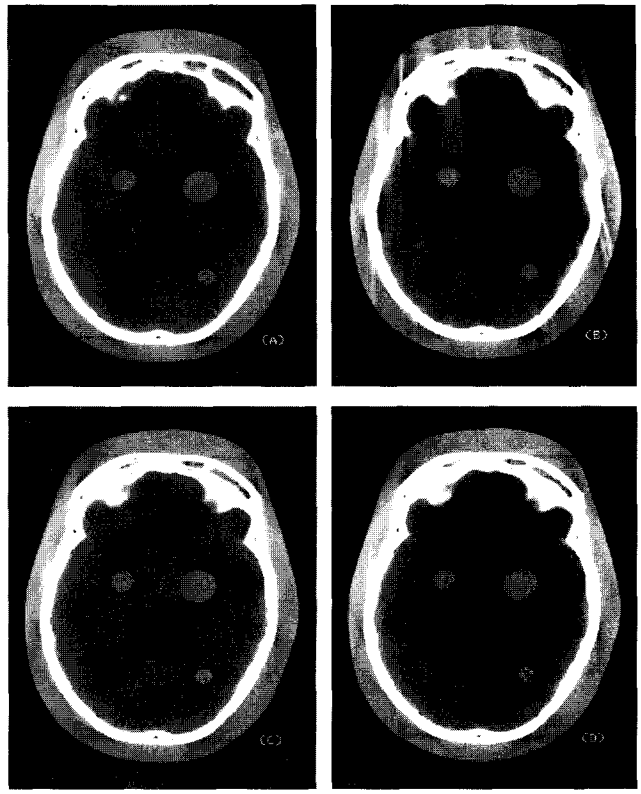

FIG. 13. Reconstructed images of a phantom. (a) axial scan mode (no table motion during scan); (b) helical without weight; (c) helical with HE; (d) helical with HI.

location, we calculated the average difference in a 10×10 pixel region between the axial image and the images generated with HE or HI algorithms. The locations and the results are depicted in Fig. 14. Note that in the majority of the locations (18 out of 21), the HI algorithm performs better than its HE counterpart, as indicated by the lower magnitude in the average difference from the "gold standard" image. A closer inspection of the two images also indicates that the HI algorithm performs slightly better in suppressing streaks near the edge of the bone. This is probably due to the fact that the weighting function used in the HI algorithm is continuous everywhere and no feathering is applied. Other phantom studies have also indicated that the HE algorithm sometimes produces a very slight shading near the starting view angle orientation. This is not the case for the HI algorithm. This can be contributed to the fact that the weights for HI are zeros at the two extreme view angles, while the weights for HE are negative.

D. Discussion

Because the weighting function is continuous everywhere for HI, some modifications or extensions can be easily made to the HI algorithm. Note that the current algorithm employs linear interpolation to arrive at the projection values at the ROR. Although the linear interpolation is easy to implement, it lacks the property of preserving high-frequency components in a signal. A natural extension to the HI algorithm is

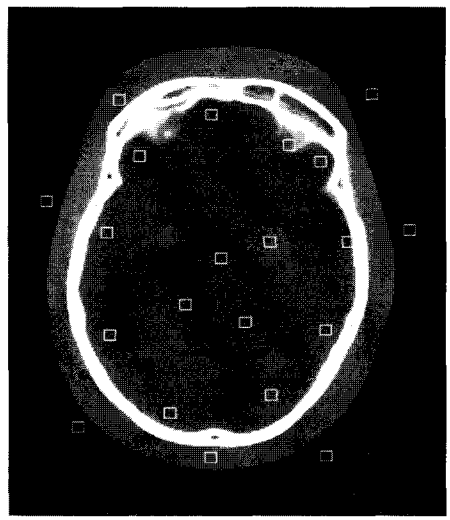

	location (X, Y)	ΔCT HE	ΔCT HI		location (X, Y)	ΔCT HE	ΔCT HI		location (X, Y)	ΔCT HE	ΔCT HI
1	345,126	43.4	37.9	8	285,235	0.6	0.5	15	215,136	−1.6	1.0
2	396,220	−47.0	−44.4	9	198, 81	−14.2	−13.9	16	240,385	0.5	0.4
3	372,142	−9.5	−12.7	10	186,210	−4.6	−3.6	17	160,398	−1.0	−1.3
4	418, 77	−2.9	−2.3	11	328,220	1.7	1.3	18	278, 96	−1.0	0.3
5	254,280	−1.8	−1.5	12	188,309	−0.3	0.1	19	328,368	0.4	0.2
6	450,209	−3.2	−3.9	13	134,179	−1.1	0.0	20	275,428	−1.1	−0.9
7	376,427	−2.3	−1.6	14	306,297	0.13	0.12	21	376,305	1.0	0.7

FIG. 14. Average CT number differences (HE—axial) and (HI—axial). HE and HI refer to the reconstructed brain phantom images using the respective algorithms and axial refers to the reconstructed brain phantom image from an axial scan mode with no table motion during the scan.

by using nonlinear interpolation schemes. The nonlinear interpolation includes the use of higher-order interpolation, as well as piecewise linear interpolation. These schemes are currently under investigation.

We have presented in detail only one example of the general approach. Other extensions to the general approach are also possible. For example, the ROR could be selected as a rectangular shape in Radon space. The weights in this region can be assigned to 1 and their complementary samples to 0. The ROR can also take other irregular shapes for the purpose of optimizing other image quality parameters.

IV. SUMMARY

In this paper, we presented a general approach to the helical reconstruction. By removing the constraint that the plane of reconstruction (POR) has to be flat and perpendicular to the z axis, a region of reconstruction (ROR) concept has been developed. This modification has added more flexibilities in defining the weighting schemes used in the reconstruction process. The added flexibility can be used to optimize system performance parameters beyond the simple artifact reduction.

For the purpose of illustration, we gave two specific examples of the ROR and derived the corresponding weighting functions. In addition, we performed detailed image quality analysis for one of the examples (HI), and compare it to one of the best helical reconstruction algorithms (HE) available to date. Although both the HE and HI algorithms use projections of 2π rotations for image reconstruction, the weighting function derived from the HI algorithm is continuous everywhere. Therefore, no feathering is required. The characteristics of the interpolation also limits the HI weights in the range $[0,1]$, which results in a better performance in terms of noise suppression. In addition, the weights employed in HI exhibit a uniform behavior in terms of its noise power, while the HE algorithm is channel dependent. This results in a better noise homogeneity for HI. We have also performed detailed comparative analysis between HE and HI in terms of their artifact reduction capability. Using the axial image (no table movement during scan) as the "gold standard," the quantitative ROI analysis has shown that the HI algorithm outperforms HE. Closer visual inspection of the images has also indicated that HI performs better than HE in terms of shading artifacts related to the starting angle and streaking

off the bones. Finally, Phantom studies have indicated that the HI algorithm performs equally well as compared to the HE in terms of their z-axis profiles and z-axis resolution.

We have also explained various ways of expanding the algorithm beyond linear interpolation and HI and PI weighting. These expansions can result in weighting functions that optimize image performances in other areas.

ACKNOWLEDGMENT

We would like to express our great appreciation for the valuable comments and suggestions made by the anonymous reviewers.

[1]J. R. Mayo, N. L. Muller, and R. M. Henkelman, "The double-fissure sign: A motion artifact on thin section CT scans," Radiology **165**, 580–581 (1987).

[2]R. D. Tarver, D. L. Conces, and J. D. Godwin, "Motion artifacts, on CT simulate bronchiectasis," Am. J. Roentgenol. **151**, 1117–1119 (1988).

[3]H. Nishimura and O. Miyazaki, "CT system for spirally scanning subject on a movable bed synchronized to x-ray tube revolution," U.S. Patent 4,789,929, 1988.

[4]I. Mori, "Computerized tomographic apparatus utilizing a radiation source," U.S. Patent No. 4,630,202, 1986.

[5]W. Kallender, W. Seissler, and P. Vock, "Single-breath-hold spiral volumetric CT by continuous patient translation and scanner rotation," Radiology **173P**, 414 (1989).

[6]P. Vock, H. Jung, and W. Kallender, "Single-breath-hold spiral volumetric CT of the hepatobillary system," Radiology **173P**, 377 (1989).

[7]P. Vock, H. Jung, and W. Kallender, "Single-breath-hold spiral volumetric CT of the lung," Radiology **173P**, 400 (1989).

[8]D. E. Dupuy, P. Costello, and C. P. Ecker, "Spiral CT of the pancreas: Comparative study," Radiology **181P**, 260 (1991).

[9]C. R. Crawford and K. King, "Computed tomography scanning with simultaneous patient translation," Med. Phys. **17**, 967–982 (1990).

[10]G. Wang and M. W. Vannier, "Longitudinal resolution in volumetric x-ray computerized tomography-analytical comparison between conventional and helical computerized tomography," Med. Phys. **21**, 429–433 (1994).

[11]P. Costello, W. Anderson, and D. Blume, "Pulmonary nodule: Evaluation with spiral volumetric CT," Radiology **179**, 875–876 (1991).

[12]M. Remy-Jardin, J. Remy, F. Giraud, and C. Marquette, "Pulmonary nodules: Detection with thick-section spiral CT versus conventional CT," Radiology **187**, 513–520 (1993).

[13]D. Ney, E. Fishman, A. Kawashima, D. Robertson, and W. Scott, "Comparison of helical and serial CT with regard to three-dimensional imaging of musculoskeletal anatomy," Radiology **185**, 865–869 (1992).

[14]D. L. Parker, "Optimal short scan convolution reconstruction for fanbeam CT," Med. Phys. **9**, 254–257 (1982).

[15]N. J. Pelc and G. H. Glover, "Method for reducing image artifacts due to projection measurement inconsistencies," U.S. Patent No. 4,580,219, 1986.

[16]D. L. Parker, V. Smith, and J. H. Stanley, "Dose minimization in computed tomography overscanning," Med. Phys. **8**, 706–711 (1981).

[17]K. King and C. R. Crawford, "Extrapolative reconstruction method for helical scanning," U.S. Patent 5,233,518, 1993.

[18]A. C. Kak, "Computerized tomography with x-ray, emission and ultrasound sources," Proc. IEEE **67**, 1245–1272 (1979).

[19]A. C. Kak and M. Slaney, *Principles of Computerized Tomographic Imaging* (Institute of Electrical and Electronic Engineers, New York, 1987).

[20]J. Namikawa, "Method of collecting data for x-ray tomography," U.S. Patent No. 4,852,132, 1989.

[21]A. Papoulis, *Probability, Random Variables, and Stochastic Processes* (McGraw-Hill, New York, 1984).